ACS APPLIED MATERIALS & INTERFACES
Research Article
www.acsami.org

Controlling Self-Assembly of Reduced Graphene Oxide at the Air−Water Interface: Quantitative Evidence for Long-Range Attractive and Many-Body Interactions

Gregory J. Silverberg,[†] Phoebe Pearce,[†,‡] and Chad D. Vecitis*[,†]

[†]School of Engineering and Applied Sciences, Harvard University, Cambridge, Massachusetts 02138, United States
[‡]Cavendish Laboratory, University of Cambridge, 19 J. J. Thomson Avenue, CB3 0HE Cambridge, United Kingdom

S *Supporting Information*

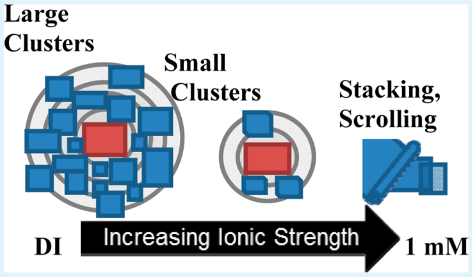

ABSTRACT: Industrial-scale applications of two-dimensional materials are currently limited due to lack of a cost-effective and controlled synthesis method for large-area monolayer films. Self-assembly at fluid interfaces is one promising method. Here, we present a quantitative analysis of the forces governing reduced graphene oxide (rGO) assembly at the air−water interface using two unique approaches: area-based radial distribution functions and a theoretical Derjaguin−Landau−Verwey−Overbeek (DLVO) interaction potential for disks interacting edge-to-edge. rGO aggregates at the air−water interface when the subphase ionic strength results in a Debye screening length equal to the rGO thickness (~1 mM NaCl), which is consistent with the DLVO interaction potential. At lower ionic strengths, area-based radial distribution functions indicate that rGO−rGO interactions at the air−water interface are dominated by long-range (tens of microns) attractive and many-body repulsive forces. The attractive forces are electrostatic in nature; that is, the force is weakened by minor increases in ionic strength. A quantitative understanding of rGO−rGO interactions at the air−water interface may allow for rational synthesis of large-area atomically thin films that have potential for planar electronics and membranes.

KEYWORDS: *graphene films, reduced graphene oxide, colloidal self-assembly, air−water interface, DLVO theory, capillary interactions*

1. INTRODUCTION

Graphene has been touted as a next-generation material for a myriad of applications due to its wide-ranging superlative properties, such as low permeability,[1] high conductivity,[2] high specific surface area, and high mechanical strength.[3] Although some applications, such as transistors and superconductors, require nearly defect-free graphene films, there are many applications where defects are not only permissible but often necessary, such as membranes, planar electronics, transparent conductors, electrodes, and composites.[4−7] However, controlled, consistent, and scalable methods for cost-effective fabrication of large monolayer graphene films required for these applications are currently unavailable.

Current methods for thin graphene film synthesis are constrained within two paradigms: bottom-up single- or few-layer chemical vapor deposition (CVD) graphene and top-down layered graphene oxide (GO) or reduced graphene oxide (rGO) films. Time- and energy-intensive CVD synthesis methods are cost-prohibitive for many industrial applications with a current price on the order of \$10 cm^{-2}. Vacuum filtration, drop-casting, spin-coating, and evaporation-induced assembly[8] of rGO sheets are much less expensive routes to graphene films.[9] However, mechanical strength,[10] specific surface area,[11] and electrical conductivity[12] are sacrificed due to poor quality of graphene sheets and limited control over their assembly resulting in stacked, folded, and aggregated sheets.[13,14]

One promising method for controlled bottom-up synthesis of industrial-scale mono- to few-layer rGO films is self-assembly at the air−water interface and Langmuir−Blodgett deposition onto the desired substrate. A number of qualitative studies have demonstrated the feasibility of this process; that is, rGO sheets are stable at the interface, and packing can be controlled by pH and surface pressure to produce tunable atomically thin films over large areas. For example, GO film porosity was observed to be a function of the applied surface pressure.[15] In acidic media, GO sheets clustered at low surface pressure and wrinkled upon compression. In basic media, GO films were more uniform at low surface pressure and stacked upon compression. Produced rGO films have demonstrated promising optical and electrical properties[16,17] with conductivities exceeding that of CVD graphene grown on a nickel substrate.[18] A quantitative examination of rGO−rGO interactions at the air−water interface has yet to be completed and is necessary to improve our understanding of the fundamental forces driving the self-assembly process at the air−water interface.

Received: December 12, 2014
Accepted: January 22, 2015
Published: January 22, 2015

DOI: 10.1021/am5087984

Here, suspended GO produced by a modified Hummer's method is first partially reduced by ultraviolet-A light (UVA; λ = 400−315 nm; predominantly 365 nm here) photolysis to reconjugate the basal plane of GO and enhance affinity for the air−water interface. In this work, rGO refers to this partially (predominantly basal plane) photoreduced GO product, not GO reduced by thermal or chemical processes as often discussed elsewhere in the literature. The rGO is deposited on the air−water interface of a Langmuir−Blodgett (LB) trough, and the aggregated film structure is examined as a function of subphase ionic strength using scanning electron microscopy (SEM). Ionic strength is used as the variable for studying rGO−rGO interactions rather than pH since effects of electrostatic shielding are deconvoluted from rGO surface-charging effects. Film structure is quantified using radial distribution functions of areal coverage. The observed phenomena are also quantitatively compared to Derjaguin−Landau−Verwey−Overbeek (DLVO) theory adapted for edge−edge interaction of atomically thin disks. The nature of the interaction forces dominating the rGO self-assembly process at the air−water interface is discussed.

2. EXPERIMENTAL SECTION

Reduced Graphene Oxide Synthesis. Graphite flakes (≥75%; 100 mesh), sulfuric acid (95−98%), potassium persulfate (≥99.0%), phosphorus pentoxide (≥98.0%), potassium permanganate (≥99.0%), hydrogen peroxide (29.0−32.0%), and hydrochloric acid (37%) were purchased from Sigma-Aldrich. rGO was synthesized via a modified Hummers' method.[19,20] First, potassium persulfate (4.2 g) and phosphorus pentoxide (4.2 g) were dissolved in concentrated sulfuric acid (30 mL) and heated to 80 °C. Graphite (5 g) was added slowly, and the temperature was maintained at 80 °C for 4.5 h. The mixture was then allowed to cool to room temperature, diluted with 600−700 mL of deionized (DI) water, and filtered through a poly(tetrafluoroethylene) membrane (pore size 0.45 μm). The solid was washed with 1 L of DI water and dried under vacuum overnight. The following day, the product was added to concentrated sulfuric acid (150 mL) at 0 °C in an ice bath. Potassium permanganate (15 g) was added slowly such that the temperature did not exceed 20 °C. The reaction mixture was heated to 35 °C for 2 h. The mixture was diluted with water (250 mL) and rapidly heated to 80 °C for two additional hours. Finally, the mixture was diluted once more with water (700 mL), quenched with hydrogen peroxide (20 mL), and cooled to room temperature.

Work up of the product involved sieving through a 300 μm standard testing sieve, filtering through a laboratory-grade glass fiber, and centrifugation (Sorvall RC-5C Plus) at 4000 rpm for 4 h. The supernatant was decanted, and the settled solid was washed with 200 mL of hydrochloric acid, 2 × 200 mL of water, and 2 × 200 mL of ethanol. Finally, the product was suspended in 200 mL of ethanol, ultrasonicated for 10 min to exfoliate the GO, dialyzed in 90% ethanol to reduce the salt content, and reduced under 365 nm irradiation (4 W) for 2 h under atmospheric conditions. Photoreduction of GO has been demonstrated by similar techniques previously reported in the literature.[21] This extent of partial photoreduction was found most effective for enhancing rGO affinity for the interface while maintaining colloidal stability. The rGO yield was 1−5% of the initial graphite mass.

Atomic Force Microscopy Analysis. Atomic force microscopy (AFM) was conducted using an Asylum MFP-3D Stand Alone AFM with OTESPA tapping mode silicon tips (300 kHz, 42 N/m). Scanning was completed at <1 Hz scanning frequency over <30 μm scan sizes. Images were analyzed, and height profiles were generated using Asylum Igor Pro software. All sheet thicknesses were measured on silica-coated silicon wafers.

X-ray Photoelectron Spectroscopy. rGO suspensions were UVA-photolyzed for 1−24 h, and a thick (5000−10 000 layers) rGO film was drop-cast onto a 1 cm^2 silicon/silica wafer for X-ray photoelectron spectroscopy (XPS) analysis. After drying overnight, both survey and high-resolution spectra were collected using a Thermo Scientific K-Alpha XPS with 400 μm spot size. Survey spectra analysis and peak deconvolution were completed using the Thermo Scientific Avantage software. The C/O ratio was calculated from the automatic peak identification function for the survey spectra (Supporting Information, Figure S1). Deconvolution of the C 1s high-resolution peak (Supporting Information, Figure S2) was completed by manually fitting peaks at binding energies of 285.0 (C−C), 286.5 (hydroxyl/epoxy), 288.0 (ketone), and 289.0 eV (carboxylate).

UV−Visible Spectroscopy. A SCINCO S-3100 was used to take UV−visible absorption measurements of rGO in a 1 mg mL^{-1} suspension over a wavelength range of 190−1100 nm. One milliliter capacity quartz cells were used with a 10 mm path length.

Boehm Titration Experiments. UV photoreduced samples were analyzed by Boehm titration. One milligram of rGO was suspended in 4 mL of 1:3 EtOH/H_2O. HCl was added slowly to lower the sample pH to 2.5. Gradually, the pH was raised to 11 using 10 μL aliquots of 50 mM NaOH. The amount of hydroxide contributing to the observed pH change was subtracted from the total hydroxide added to the solution to determine the number of surface groups that were deprotonated during the titration. The functional groups were differentiated based on pK_a and the observed pH of deprotonation as shown in Supporting Information, Figure S3.

Reduced Graphene Oxide Assembly at Air−Water Interface. A Kibron MicroTroughXS LB trough was used to cast and deposit the two-dimensional (2D) rGO films. The surface pressure was measured using the Wilhelmy method with a thin alloy wire. The surface was initially aspirated to remove any contamination until $\Delta\pi$ upon full compression was less than 1 mN m^{-1}. Then, typically ~0.1 mg of rGO suspended in 9:1 EtOH/H_2O was slowly deposited onto 2000 mm^2 of air−water interface. This is equivalent to 1 μg or 25 cm^2 of rGO dispensed per cm^2 of air−water interface; however, only ~1% of the deposited rGO remained at the air−water interface. Addition of rGO suspension to the air−water interface typically decreased the surface tension of the interface to ~65−70 mN m^{-1}. However, after 45 min to allow for ethanol evaporation and thermal equilibration, the measured surface tension increased to that of water, 72.8 mN m^{-1}. Films were not compressed in any of the experiments described in this work. This indicates that at low surface coverage and without compression, particles did not climb the meniscus of the Wilhelmy needle and in turn did not show a measurable change in surface tension. Therefore, nonuniform particle distribution made a measure of surface tension uninformative in this case, so bulk surface coverage was calculated after deposition instead. Subphase ionic strength was controlled by varying the concentration of dissolved NaCl.

A 500 μm thick silicon/silica wafer was cleaned by an ethanol/water rinse followed by 15 min of bath ultrasonication. The wafer was hydrophilic with a contact angle of 45 ± 6°. This contact angle was constant regardless of the ionic strength of the water. This cleaning process was deemed sufficient since cleaning with piranha solution resulted in a contact angle of 40 ± 3°. The rGO film was deposited onto the silicon/silica wafer using the LB technique by vertically dipping the substrate perpendicularly to the subphase and removing at a speed of <1 mm min^{-1}.

Scanning Electron Microscopy. SEM imaging was conducted using a Zeiss Supra55VP FESEM at 5 kV using the inlens detector. For the long-range attractive and many-body repulsive forces, images of 2000× and 10 000× magnification were used, respectively, to provide the necessary resolution. Bulk coverage fraction was found by averaging over all images at each magnification.

Film Structure Analysis. rGO size distributions, radial distribution functions, and the fraction of particles aggregated were determined by SEM image analysis of deposited films. rGO assembly at the air−water interface was inferred by observing the structure of films after deposition. As described in detail below, the deposition and drying process may conceivably play a role in film structure, but since they were held constant for all experiments, the major contributing factor to differences in film structure is the ionic strength of the

DOI: 10.1021/am5087984
ACS Appl. Mater. Interfaces 2015, 7, 3807−3815

subphase. Standard Matlab functions were used for image analysis. SEM images were converted to binary images using the global image threshold function. Aggregated particles were separated with the watershed function using the distance transform of a binary image after suppressing all minima in the transform less than 15 intensity units deep (Supporting Information, Figure S4). Particle centroids and boundaries were marked and used to calculate the rGO size distribution and radial distribution functions. The fraction aggregated is the number fraction of particles that are separated from at least one neighbor by less than one pixel (<9 nm). The distance separating two particles is defined as the portion of the centroid-to-centroid line that does not lie within either particle (Figure S4). Because of rGO shape anisotropy, these measurements will have a large standard deviation necessitating the use of an area-based radial distribution function.

The discrete area-based radial distribution function, $g(r_i)$, is calculated by drawing a series of i concentric circles of radii $r_i = r_1 + (i - 1)\delta r$ around each particle, where r_1 is the longest distance from the centroid of the particle to its boundary and δr is the spacing of the annuli (Figure 1). The fraction of available area covered by rGO in each annulus of inner radius r_{i-1} and outer radius r_i is defined as $\phi(r_i)$ (eq 1). The $\phi(r_i)$ value decays to the bulk coverage fraction, ϕ_{bulk}, as the radius of the annuli tends toward infinity (eq 2).

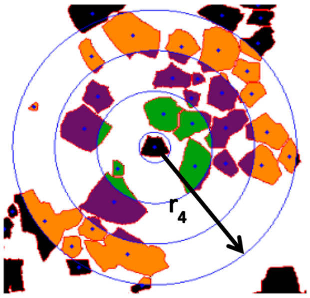

Figure 1. Graphic illustrating the area-based radial distribution function, $g(r_i)$. Coverage in annulus r_1, r_2, and r_3 is colored in green, purple, and orange, respectively.

$$\phi(r_i) = \frac{A_{\text{occ}}(r_i)}{\pi r_i^2 - \pi r_{i-1}^2} \tag{1}$$

$$\lim_{r_i \to \infty} \phi(r_i) = \phi_{\text{bulk}} \tag{2}$$

The area-based radial distribution function, $g(r_i)$, is $\phi(r_i)$ normalized to the bulk coverage fraction (eq 3) and is an indication of rGO concentration or depletion in each annulus, thus indicating the direction of force within that annulus. Again, this is a more fitting measure of particle distribution for this system than the classical radial distribution function based on number density because of the heterogeneity in rGO shape and size.

$$g(r_i) = \frac{\phi(r_i)}{\phi_{\text{bulk}}} \tag{3}$$

where $\phi(r_1)$ is defined as the "nearest neighbor" coverage fraction; the coverage fraction within a circle of radius r_1 excluding the central particle. $\phi(r_1)$ is used to quantify shorter-range interactions in this system. The ratio $g(r_1) = \phi(r_1)/\phi_{\text{bulk}}$ is plotted against ϕ_{bulk} for analysis of many-body interactions.

3. RESULTS AND DISCUSSION

Reduced Graphene Oxide Characterization. The majority (80–90%) of rGO sheets at the air–water interface have a characteristic thickness of 1.5 nm by AFM (Figure 2), which falls within the range of monolayer thicknesses reported for GO.[22−24] Measured thicknesses larger than the theoretical values of 0.8–1.0 nm for monolayer GO are attributed to liquid water trapped between the substrate and the rGO sheet. The rGO size distribution at the air–water interface is Gaussian with a mean equivalent radius of 1.0–1.1 μm (Figure 3).

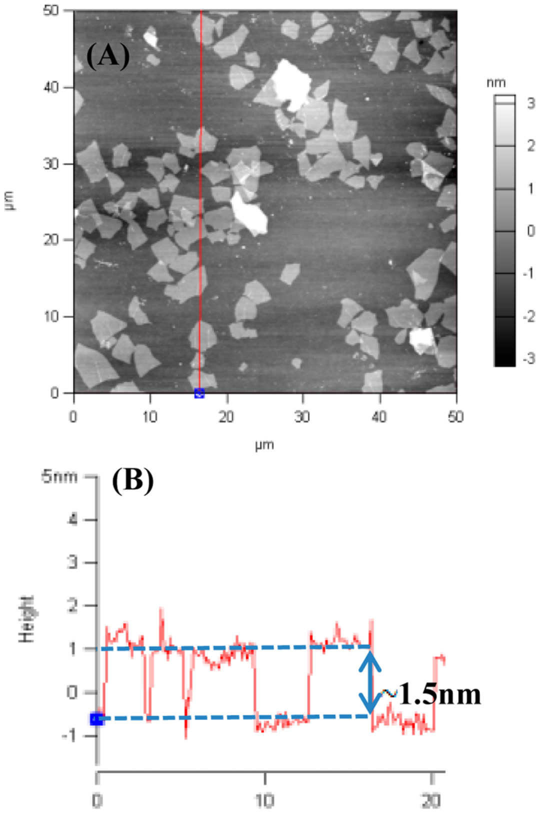

Figure 2. AFM height measurement of rGO. (A) AFM image and (B) height profile illustrating the uniform 1.5 nm step height of rGO deposited on a silica wafer.

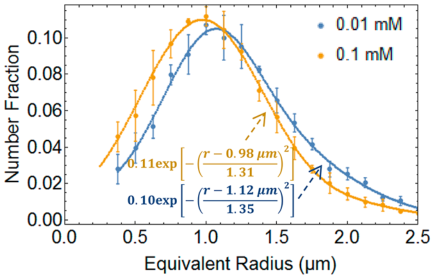

Figure 3. rGO size distribution at the air–water interface. Particle size distribution as determined by Matlab from analysis of SEM images. The size distributions are Gaussian.

Surface charge and functionalization of the photoreduced GO is analyzed by UV–visible spectroscopy, XPS, and Boehm titration.[25] UV photoreduction increases rGO absorbance across the UV–visible–near-IR spectrum with increasing exposure time indicating an increase in sp^2 conjugation of the basal plane (Figure 4).[26,27] XPS spectra indicate slight deoxygenation (C/O ratio increases from 1.9 to 2.4), loss of ketone/hydroxyl/epoxy surface groups, and increased C–C bonding, in agreement with increased sp^2 conjugation (Figure 5A). The Boehm titration data indicate only a small decrease (<10–20%) in surface charge density with increasing photolysis time (Figure 5B), confirming the loss of oxygen functional groups with high pK_a, such as ketone and epoxy groups, as the

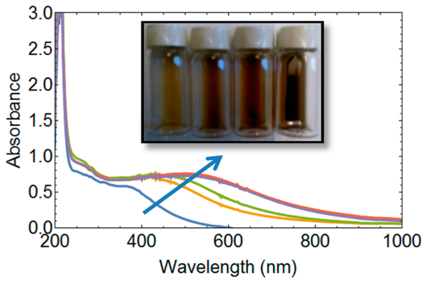

Figure 4. rGO UV−visible absorption spectrum as a function of irradiation time. Arrow indicates increase in irradiation time: 0 (blue), 2 (orange), 10 (green), 24 (red) h with 365 nm, and purple 24 h at 365 nm followed by 6 h at 254 nm. (inset, left to right) Images of 0, 2, 10, and 24 h photoreduced GO in ethanol with 365 nm.

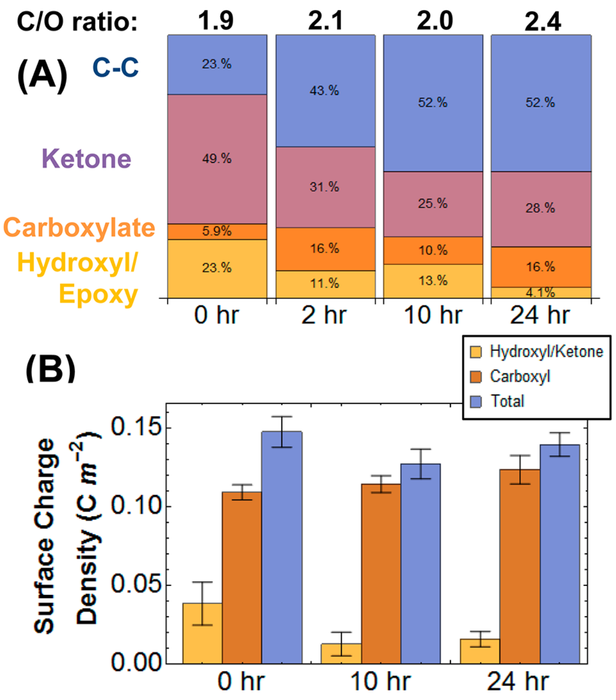

Figure 5. Effect of photoreduction on rGO functional groups and charge. (A) XPS characterization of the oxygen functionalities with increasing photoreduction was completed by C 1s peak deconvolution using 285.0, 286.5, 288.0, and 289.0 eV to quantify C−C, hydroxyl, ketone, and carboxyl bonding, respectively. C/O ratios were calculated from survey spectra. (B) Surface-charge analysis by Boehm titration to determine concentration of low pK_a ($0 < pK_a < 14$) surface groups with increasing photoreduction.

dominant effect of photoreduction. Carboxylate groups are the main contributors to surface charge at neutral pH and remain largely unaffected by 365 nm photoreduction. Surface charge analysis was not performed on the 2 h reduced sample due to the insignificant change in surface charge between the extrema (0 and 24 h reduced; Figure 5A), and thus it can be inferred that the surface charge of the 2 h reduced sample would also be insignificantly different from the extrema. Previous studies on rGO structure indicate that carboxylate and hydroxyl functionalities are located at the sheet edges, while ketone and epoxy groups are located on the basal plane.[28,29] Thus, the rGO used here consists of a basal plane with large regions of extended aromaticity surrounded by charged oxygen-based functional groups at the rGO edges. Photoreduced GO will have enhanced affinity for the air−water interface while retaining colloidal stability. Two hours of photoreduction was selected here for colloidal stability, limited rGO wrinkling, and high surface activity. Although the change in C/O ratio is slight (∼10%) after UVA photolysis, partial reduction is substantiated by the increasing UV−visible absorbance of the rGO suspension (Figure 4) and increased surface activity, which are both indicative of sp^2 reconjugation of the basal plane.

Analysis of rGO Aggregation at the Air−Water Interface. The qualitative behavior of rGO at the air−water interface is altered (Figure 6) by minor variations in the

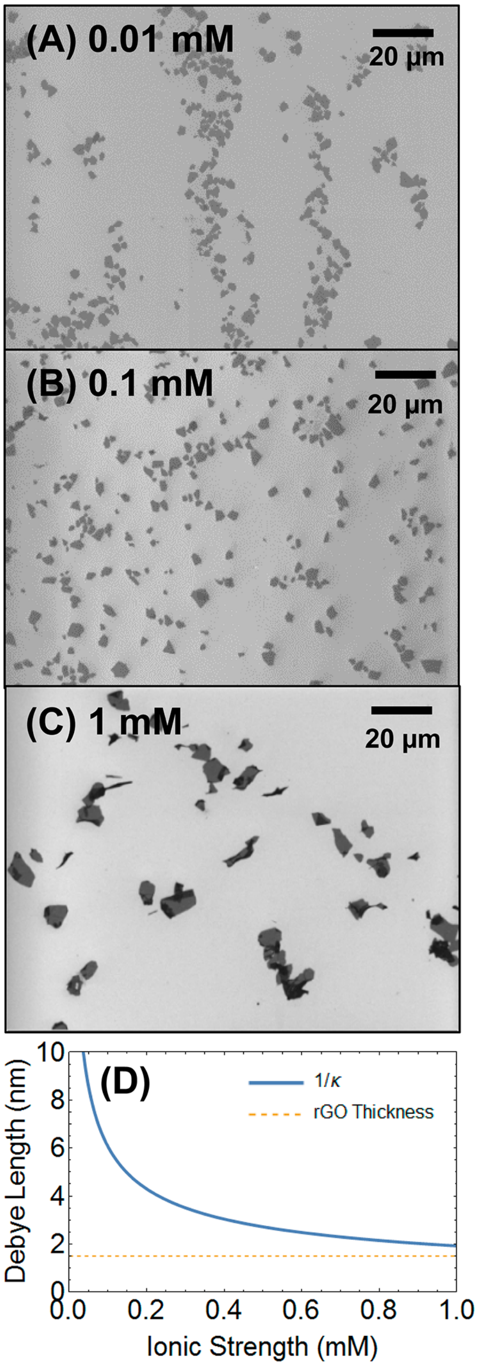

Figure 6. SEM images of rGO LB films at varying subphase ionic strength. Subphase electrolyte composition of (A) 0.01, (B) 0.1, and (C) 1 mM NaCl. (D) The Debye−Hückel screening length as a function of ionic strength.

subphase ionic strength. The pH of the subphase in all experiments is constant at 5.5–6.0 under standard atmospheric conditions. Only carboxylate groups, which constitute ~75% of the low pK_a (<14) surface groups, will be deprotonated under these conditions resulting in an rGO surface charge of 0.10–0.11 C m^{-2}. At the lowest ionic strength of 0.01 mM NaCl (that measured for rGO in DI water), the rGO sheets tend to self-assemble into large clusters, and there is minimal aggregation (<10% of particles), which is indicative of a local secondary minimum in potential energy due to a balance between long-range attractive and short-range repulsive forces. At a slightly higher ionic strength of 0.1 mM NaCl, the rGO form smaller clusters of 10 particles or fewer. At a still higher ionic strength of 1 mM NaCl, two modes of rGO aggregation are observed; at low surface coverage fraction, the rGO tend to self-aggregate forming folded or scrolled structures (Supporting Information, Figure S5); at high surface coverage fraction, the rGO tend to stack and remain flat at the interface (Supporting Information, Figure S6). The average particle size at the interface at 1 mM subphase ionic strength is visibly larger due to the aggregation of small particles. As shown in Figure 6D, the Debye screening length, $\kappa^{-1} = [((8\pi e^2 n_\infty)/(kT\varepsilon))]^{-1/2}$ (where k is the Boltzmann constant, n_∞ is the bulk ionic strength, e is the elementary charge, ε is the permittivity of the medium, and T is ambient temperature) is nearly equal to the sheet thickness at 1 mM ionic strength. Thus, when the Debye screening length is near the rGO sheet thickness, the electrolyte screening induces aggregation, that is, rGO stacking, scrolling, and folding.

The observed changes in cluster size and onset of aggregation are believed to be the result of rGO assembly at the air–water interface, not the ethanol drying process prior to deposition or the dewetting process after deposition. The rGO aggregation behavior is significantly different at each ionic strength condition, even though changes in ionic strength are slight (<1 mM). The influence of the Marangoni effect on rGO aggregation would be unchanged for each condition because the same volume of ethanol is added to the surface of the subphase and because the same ethanol evaporation conditions are used for each sample. Additionally, the contact angle of the subphase with the substrate remains constant at 45° ± 6° under all ionic strength conditions. If ethanol drying or spinodal dewetting were the dominant contributing factors causing the observed clustering and aggregation behavior, then the film structure would be similar at all ionic strengths. Therefore, the large differences in behavior as a function of subphase ionic strength must be due to rGO particle–particle interactions at the air–water interface.

As previously noted, even at lower ionic strengths, some aggregation (<10% of particles) in the form of edge-to-edge contact is observed (Supporting Information, Figure S7), which is indicative of an energy barrier that is 5–10 times the thermal energy. The magnitude of the energy barrier is estimated using eq 4 and the stability ratio, W, of ~2–200, where R is disk radius (the mean of the Gaussian distribution: 1 μm), and $\phi_{\max}$ is the height of the energy barrier (J).[30]

$$W \approx \frac{1}{2\kappa R}\exp\left[\frac{\phi_{\max}}{kT}\right] \tag{4}$$

The high surface charge density of rGO, ~1 negative charge per 1.25 nm^2, results in strong electrostatic coupling between the rGO and the electrolyte and in turn failure of the linearized Poisson–Boltzmann equation. However, outside the screening length, the linearized Poisson–Boltzmann equation can be used if the surface charge is renormalized to account for the surface charge limits due to strongly bound electrolyte ions (eq 5):[31]

$$Z_{\text{eff}}^{\text{sat}} = \frac{R}{l_{\text{B}}}\frac{2\kappa R}{1 - \exp(-\kappa R)} \tag{5}$$

where l_{B} is the Bjerrum length. This assumption is confirmed by calculation of the effective saturated charge density, that is, 1 negative charge per 25 nm^2, which is substantially lower than the bare surface charge. The saturated effective surface charge assumes constant surface potential, which here is ca. −41 mV using the Gouy–Chapman equation.[30] To calculate the theoretical energy barrier, the geometry of the particles is critically important. No cohesive DLVO-based theory exists for edge-to-edge interactions between thin disks. Thus, the rGO–rGO interaction potential was first estimated using the spherical solution for the electrostatic[32] and van der Waals[33] potentials, eqs 6 and 7:

$$\begin{aligned}\text{vdW}(r, R_1, R_2) = \frac{-A_{\text{H}}}{6}\Bigg[&\frac{2R_1R_2}{h^2 + 2R_1h^2 + 2R_2h^2}\\ &+ \frac{2R_1R_2}{h^2 + 2R_1h^2 + 2R_2 + 4R_1R_2}\\ &+ \log\frac{h^2 + 2R_1h^2 + 2R_2}{h^2 + 2R_1h^2 + 2R_2h^2 + 4R_1R_2}\Bigg]\end{aligned} \tag{6}$$

$$\text{ES}(r, R_1, R_2) = \frac{128\pi R_1R_2n_\infty kT\gamma_1\gamma_2}{(R_1 + R_2)\kappa^2}e^{-\kappa h} \tag{7}$$

where A_{H} is the Hamaker's constant, estimated by McAllister et al. for GO using Lifshitz theory in the nonretarded regime[34] to be 2.37 × 10^{-21} J, h is the edge-to-edge separation, and γ_1 and γ_2 are the reduced surface potentials. As shown in Figure 7A, an

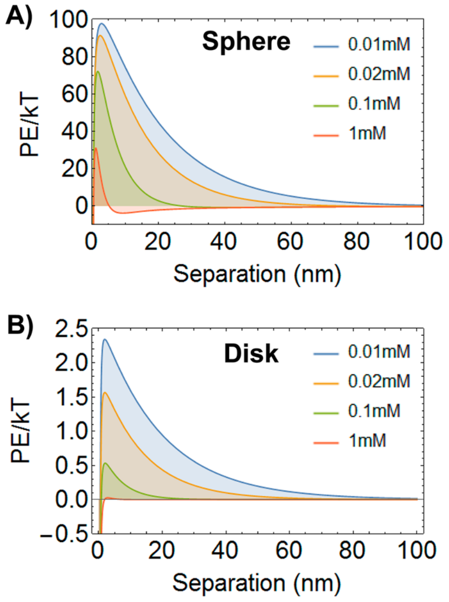

Figure 7. rGO interaction potentials based on DLVO theory for spheres and disks. (A) Spherical interaction potential from eqs 6 and 7. (B) DLVO theory extended to disks using eqs 11 and 12. Note the difference of y-axis scales in A and B.

energy barrier of 30−100 times the thermal energy for all conditions is calculated using bulk water conditions, which would not result in any aggregation. Thus, this formulation of DLVO theory is clearly insufficient to describe rGO−rGO interactions at the air−water interface.

To quantify the van der Waals attractive force for the thin disk geometry, the pairwise integration approach first proposed by Hamaker for spheres[33] was adapted. The face-to-face van der Waals force was not considered because without compression the rGO particles are irreversibly adsorbed to the air−water interface.[35] The face-to-face interaction observed at 1 mM subphase ionic strength is a result of electrolyte screening that allows for face-to-face interaction prior to or during the adsorption process. After adsorption, the particles will not interact in a face-to-face geometry, and thus this does not need to be considered in relation to aggregate formation at the interface. Therefore, only the rGO edge-to-edge geometry was considered. Briefly, this approach assumes that all atoms of particle 1 occupying a volume $\mathrm{d}v_1$ a fixed distance r from an atom of particle 2 interact with the same attractive potential. The inverse is also true for all atoms of particle 2 occupying volume $\mathrm{d}v_2$ a fixed distance from an atom of particle 1. This potential decays with r^{-6} for two induced dipoles, where q is the number density of atoms in the material, and λ is the van der Waals constant (proportional to polarizability; eq 8).

$$E = -q^2\lambda \int \mathrm{d}v_1 \int \mathrm{d}v_2 \frac{1}{r^6} \tag{8}$$

By first evaluating the integration over $\mathrm{d}v_2$, the potential of a single atom at point P due to its interaction with particle 2 is given by eq 9, where δ is the thickness of the disk, and the other parameters are given in Figure 8.

$$E_{\mathrm{P}} = -2\delta\lambda q \int_{R-R_2}^{R+R_2} \frac{r\theta_0(r, R, R_2)}{r^6}\mathrm{d}r \tag{9}$$

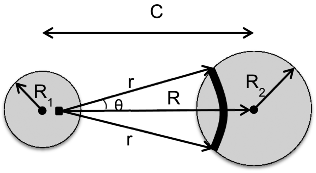

Figure 8. Integration geometry for calculating the disk-shaped van der Waals potential. Two disks of radii R_1 and R_2 and thickness δ are separated by a distance C. Atom P is a distance R from the center of particle 2. Circular segments equidistant from each other are integrated over the r^{-6} dependence of the van der Waals interaction potential.

The r dependence of θ_0 for thin circular disks is found geometrically to be $\theta_0(r, R, R_2)$ = arccos $((r^2 - R_2^2 + R^2)/(2rR))$. After integrating E_{P} for each equidistant circular segment over particle 1 (eq 10), the full interaction pair potential for thin disks is found (eq 11), where $A_{\mathrm{H}} = \pi^2 q^2 \lambda$ is the Hamaker constant, and r is now the center-to-center separation distance, replacing the constant C used in the integration.

$$E = 2\delta q \int_{C-R_1}^{C+R_1} E_{\mathrm{P}} R\theta_0(R, C, R_1)\mathrm{d}R \tag{10}$$

$$\mathrm{vdW}(r, R_1, R_2) = -A_{\mathrm{H}}\delta^2\left[\frac{R_1^{\,2}R_2^{\,2}(R_1^{\,4} - 2r^4 + r^2R_2^{\,2} + R_2^{\,4} + R_1^{\,2}(r^2 - 2R_2^{\,2}))}{2(R_1^{\,4} + (r^2 - R_2^{\,2})^2 - 2R_1^{\,2}(r^2 + R_2^{\,2}))^{5/2}}\right] \tag{11}$$

The electrostatic potential previously solved for disks to model clay suspensions was employed for the repulsive component of disk-shaped DLVO (eq 12).[31]

$$\mathrm{ES}(r, R_1, R_2) = 4Z_{\mathrm{eff}}^{\mathrm{sat}}(R_1)Z_{\mathrm{eff}}^{\mathrm{sat}}(R_2)l_{\mathrm{B}}\frac{I_1(\kappa R_1)}{\kappa R_1}\frac{I_1(\kappa R_2)}{\kappa R_2}\left[\frac{e^{-\kappa h}}{r}\right] \tag{12}$$

where I_1 is the modified Bessel function of the first kind. A plot of the rGO−rGO interaction potential using the same assumptions as the spherical case is displayed in Figure 7B, and the energy barrier to aggregation more closely matches experimental observation. Although the height of the energy barrier is a factor of 2−5 lower than that estimated by stability ratios, this could be attributed to variations in parameters (dielectric constant, ionic strength, etc.) at the air−water interface as compared to the bulk, as discussed in detail below. The energy barrier is negligible at 1 mM ionic strength, which is consistent with observed aggregation. The van der Waals attractive force is also much lower in magnitude, which is reasonable in light of the two-dimensionality and thus low mass of rGO. For example, circular rGO of diameter 2 μm has a mass of ~1 fg, whereas a graphite sphere of similar diameter has a mass of ~10^4 fg.

The dielectric constant at the air−water interface varies from that of air (2) to that of water (80) over the first 20 nm of the interface.[36] Additionally, it is known that monovalent cations and small anions are depleted within the first 1 nm of the interface.[37] Decreasing the dielectric constant will decrease the height of the energy barrier, and in contrast, decreasing the ionic strength will increase the height of the energy barrier. Presently, it is not possible to quantitatively determine the magnitude of each effect; that is, ion depletion at the interface and precise position of rGO at the interface are both unknown. Even so, DLVO theory for disk−disk edge−edge interactions derived here approximates the rGO−rGO energy barrier at the air−water interface significantly better than sphere−sphere interactions.

Long-Range Attractive Interactions. Quantification of the range of interactions for particles with extreme shape anisotropy is inherently difficult. Classical calculations using particle trajectories[38] or radial distribution functions based on number density require spherical symmetry of colloidal interactions. However, a quantitative radial distribution function based on areal coverage fraction avoids this symmetry requirement and may offer more insight into interaction phenomena for highly shape anisotropic particles such as rGO at the air−water interface. For randomly distributed particles, the coverage fraction any annulus a distance r away from each particle would be constant and similar to the bulk coverage fraction for all r. If rGO−rGO attractive interactions are significant within the measured range, the ratio of coverage fraction to the bulk coverage fraction, $g(r_i)$, will be >1 and will decay to the bulk coverage fraction at $r_i \to \infty$. Similarly, if rGO−rGO repulsive interactions are significant within the measured range, there will exist a local minimum ($g(r_i) < 1$). The height of the peak or depth of the valley is a measure of rGO concentration or depletion within that range as compared to the bulk. The width of the peak is a measure of the range of interactions. More than 30 SEM images at 2000× magnification were taken at each condition, and radial distribution functions $g(r)$ were calculated independently for each individual image. Samples were selected such that the average bulk surface coverage was similar for the average radial distribution function calculations. For example, at the low ionic strength condition (0.01 mM), the bulk surface coverage ranged from 2 to 35% with a mean of 13 ± 9%, and at the high ionic strength condition, the bulk surface coverage ranged from 3 to 39% with a mean of 16 ± 8%. The average radial distribution function with standard deviation for each ionic strength condition is displayed in Figure 9. When the subphase ionic strength is low, 0.01 and 0.02 mM, the coverage fraction is found to be several times (4−8) higher than the bulk over the first 1−20 μm from any particle. This is an indication of the self-assembly of large rGO clusters due to dominant long-range attractive forces. Repulsive forces are present, but not observed because their range is shorter than those measured here (<1 μm). At higher ionic strength (0.1 mM), the clusters are smaller (<10 μm), their coverage fraction (2) is closer to the bulk, and the range of the attractive force is diminished. Typically the opposite effect is observed with increasing ionic strength due to electrolyte screening of electrostatic repulsion.

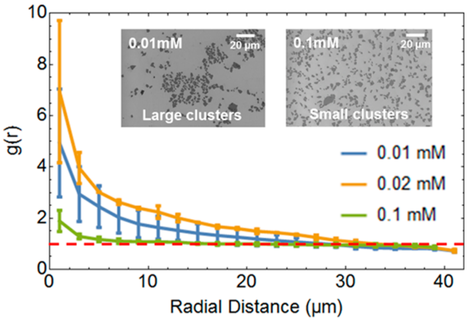

Figure 9. RDF quantification of long-range rGO attractive forces at the air−water interface. Areal coverage-based radial distribution functions are determined using SEM images and Matlab at varying ionic strength. (inset, left) SEM image of self-assembled large clusters at low ionic strength. (inset, right) SEM image of smaller clusters at moderate ionic strength.

The origin of the long-range attractive force is not likely van der Waals since the effect of a van der Waals force would likely increase with increasing ionic strength. Additionally, the van der Waals interaction potential for disk-shaped particles is negligible at large distances. Even if the Hamaker's constant is increased to an unreasonably high value (10^{-17} J), that is, 2 orders of magnitude greater than typical values, the attractive forces are still negligible beyond 100 nm particle separation distances. Thus, a non-DLVO attractive force such as a hydrophobic or capillary interaction due to deformation of the interface (thermal fluctuations, shape anisotropy, particle wetting, surface roughness, or electric field) is likely dominating rGO interactions at the air−water interface. In general, hydrophobic interactions[39] and thermal fluctuations[40] at the air−water interface will be too short-range (<100 nm) to account for the observed attractive forces. Particle wetting or "immersion forces" are observed only in thin liquid films due to the existence of a meniscus around the particle. Since rGO is an atomically thin and thus an extremely low mass particle that is lying on top of an incompressible fluid, an immersion force is also not likely to be the correct explanation. Surface roughness is also an unlikely mechanism due to the atomic dimension of rGO. Therefore, the two most likely explanations for the observed phenomenon are shape anisotropy[41,42] and/or electric-field induced[43,44] deformation of the interface as both phenomenon have been previously observed to induce long-range capillary attractions. Although the electric-field induced interface deformation is controversial, it is the only electrolyte-dependent long-range attractive force known to the authors. We hypothesize that the long-range clustering is a result of a combination of the two effects since shape anisotropy would result in nonuniform electric charge as well as an irregular wetting angle.[42]

Repulsive Many-Body Interactions. Qualitatively, as rGO surface coverage fraction increases, that is, as nearest neighbor number increases, neighboring rGO particles are observed to be stabilized from aggregation; that is, nearest neighbor distance also increases, due to repulsive many-body interactions. To quantify these interactions, the "nearest neighbor coverage fraction", $g(r_1)$, is defined as the coverage fraction within a circle that circumscribes each particle, excluding the area of the particle itself. This is the first "bin" of the area-based radial distribution function. To analyze the first "bin", more than 30 SEM images at 5000× magnification were taken of each sample, and nearest-neighbor coverage fractions were calculated independently for each individual image. The nearest-neighbor coverage fraction does not increase proportionally with the bulk coverage fraction, as shown in Figure 10. In fact, at low coverage fraction, rGO has fewer neighbors with a lesser separation distance, and at high coverage fraction, rGO has more neighbors with a greater separation distance. To support these data, the fraction of rGO aggregated, that is, in contact with another rGO as observed by SEM, is plotted as a function of coverage fraction in Figure S7. The fraction of rGO aggregated decreases with increasing coverage fraction confirming the observation of a many-body interaction. Therefore, the effective energy barrier to aggregation increases both in magnitude and range with increasing bulk coverage fraction. Previous studies have shown that many-body repulsion becomes dominant as deformable disks approach the compressibility limit.[45] The observation of many-body effects in this system may be consistent with these results since local area-confinement is

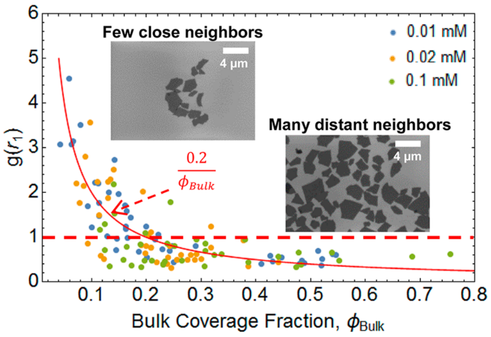

Figure 10. Quantification of rGO many-body interactions at the air−water interface. The ratio of nearest-neighbor coverage fraction to bulk coverage fraction ($g(r_1)$) is plotted versus the bulk coverage fraction (ϕ_{bulk}). (inset, left) SEM image of tightly packed rGO sheets at low coverage fraction. (inset, right) SEM image of loosely packed rGO at high coverage fraction.

introduced via the long-range capillary attraction. However, the many-body interaction is observed at all subphase ionic strengths making its nature ambiguous. For example, the many-body interaction may be electrostatic in nature if the shielding required to significantly diminish this force occurs at higher ionic strengths than those evaluated here. Alternatively, the interaction may be the result of a repulsive capillary interaction. In either case, when casting an rGO membrane at the air−water interface, many-body interactions may in fact prevent folding, wrinkling, and crumpling of an rGO thin film, a problem observed for other synthesis techniques.[15]

4. CONCLUSIONS

rGO is observed to lie flat on the air−water interface and remain stable from aggregation at ionic strengths below 1 mM. At and above this ionic strength, rGO self-aggregates by stacking, folding, and scrolling. This phenomenon is hypothesized to be a result of the Debye−Hückel screening length being on the order of magnitude of the thickness of the rGO sheets. This hypothesis is substantiated by the disappearance of the rGO−rGO energy barrier at 1 mM ionic strength when using DLVO theory adapted for edge−edge interactions of atomically thin disk-shaped particles. rGO clusters of 20 μm and larger are observed to self-assemble at ionic strengths $\leq$0.02 mM as quantified by an area-based radial distribution function and are indicative of a long-range attractive force. The long-range attractive force diminishes at 0.1 mM as observed by a decrease in cluster size and is hypothesized to be non-DLVO in nature but induced by the rGO electric field and shape anisotropy. A many-body rGO−rGO interaction was also observed in which nearest-neighbor coverage fraction and aggregated fraction decrease with increasing rGO surface density. This effect diminishes rGO aggregation at the interface and enhances film uniformity. Thus, observations made here contribute to the recent debate about the nature of particle−particle interactions at air−water interfaces;[44,46] that is, long-range interactions (10s of microns) are electrostatic in nature. The quantitative analysis of rGO aggregation at the air−water interface may also allow for rational optimization of industrial scale thin (nanometers) film synthesis. For example, to prevent rGO aggregation, the Debye screening length must exceed the sheet thickness (<1 mM) of monovalent salt. However, a slight increase in ionic strength (0.1 mM) will weaken the long-range attractive force resulting in rGO clustering and in turn enhance film uniformity. These results provide new insight into the self-assembly of 2D materials at air−water interfaces, a promising method for production of industrial scale nanometer thin films.

■ ASSOCIATED CONTENT

Supporting Information

Raw XPS and titration data, an example of the Matlab watershed function and center-to-center distance measurement, and AFM data. This material is available free of charge via the Internet at http://pubs.acs.org.

■ AUTHOR INFORMATION

Corresponding Author

*E-mail: vecitis@seas.harvard.edu. Phone: (617) 496-1458.

Notes

The authors declare no competing financial interest.

■ ACKNOWLEDGMENTS

This work was supported by a Faculty Grant for Exploratory Research from the Harvard University Center for the Environment. It was performed in part at the Center for Nanoscale Systems (CNS), a member of the National Nanotechnology Infrastructure Network (NNIN), which is supported by the National Science Foundation under NSF Award No. ECS-0335765. CNS is part of Harvard University. G.J.S. would like to acknowledge the financial support of the National Science Foundation Graduate Research Fellowship, as well as the helpful discussions with Professors K. Bertoldi, M. Brenner, F. Spaepen, and V. Manoharan.

■ REFERENCES

(1) Bunch, J. S.; Verbridge, S. S.; Alden, J. S.; van der Zande, A. M.; Parpia, J. M.; Craighead, H. G.; McEuen, P. L. Impermeable Atomic Membranes from Graphene Sheets. *Nano Lett.* **2008**, *8*, 2458−2462.

(2) Neto, A. C.; Guinea, F.; Peres, N.; Novoselov, K. S.; Geim, A. K. The Electronic Properties of Graphene. *Rev. Mod. Phys.* **2009**, *81*, 109.

(3) Lee, C.; Wei, X.; Kysar, J. W.; Hone, J. Measurement of the Elastic Properties and Intrinsic Strength of Monolayer Graphene. *Science* **2008**, *321*, 385−388.

(4) Zhu, Y.; Murali, S.; Cai, W.; Li, X.; Suk, J. W.; Potts, J. R.; Ruoff, R. S. Graphene and Graphene Oxide: Synthesis, Properties, and Applications. *Adv. Mater.* **2010**, *22*, 3906−3924.

(5) Wang, X.; Zhi, L.; Müllen, K. Transparent, Conductive Graphene Electrodes for Dye-Sensitized Solar Cells. *Nano Lett.* **2007**, *8*, 323−327.

(6) Shao, J.-J.; Li, Z.-J.; Zhang, C.; Zhang, L.-F.; Yang, Q.-H. A Wavy Graphene/Platinum Hybrid with Increased Electroactivity for the Methanol Oxidation Reaction. *J. Mater. Chem. A* **2014**, *2*, 1940−1946.

(7) Guo, F.; Silverberg, G.; Bowers, S.; Kim, S.-P.; Datta, D.; Shenoy, V.; Hurt, R. H. Graphene-Based Environmental Barriers. *Environ. Sci. Technol.* **2012**, *46*, 7717−7724.

(8) Chen, C.; Yang, Q.-H.; Yang, Y.; Lv, W.; Wen, Y.; Hou, P.-X.; Wang, M.; Cheng, H.-M. Self-Assembled Free-Standing Graphite Oxide Membrane. *Adv. Mater.* **2009**, *21*, 3007−3011.

(9) The Price of Graphene. Graphenea; http://www.graphenea.com/pages/graphene-price#.VACZpfldVUU (accessed 08/29).

(10) Suk, J. W.; Piner, R. D.; An, J.; Ruoff, R. S. Mechanical Properties of Monolayer Graphene Oxide. *ACS Nano* **2010**, *4*, 6557−6564.

(11) Stoller, M. D.; Park, S.; Zhu, Y.; An, J.; Ruoff, R. S. Graphene-Based Ultracapacitors. *Nano Lett.* **2008**, *8*, 3498−3502.

(12) Gómez-Navarro, C.; Weitz, R. T.; Bittner, A. M.; Scolari, M.; Mews, A.; Burghard, M.; Kern, K. Electronic Transport Properties of Individual Chemically Reduced Graphene Oxide Sheets. *Nano Lett.* **2007**, *7*, 3499−3503.

(13) Park, S.; Ruoff, R. S. Chemical Methods for the Production of Graphenes. *Nat. Nanotechnol.* **2009**, *4*, 217−224.

(14) Dikin, D. A.; Stankovich, S.; Zimney, E. J.; Piner, R. D.; Dommett, G. H. B.; Evmenenko, G.; Nguyen, S. T.; Ruoff, R. S. Preparation and Characterization of Graphene Oxide Paper. *Nature* **2007**, *448*, 457−460.

(15) Kim, F.; Cote, L. J.; Huang, J. Graphene Oxide: Surface Activity and Two-Dimensional Assembly. *Adv. Mater.* **2010**, *22*, 1954−1958.

(16) Cote, L. J.; Kim, J.; Zhang, Z.; Sun, C.; Huang, J. Tunable Assembly of Graphene Oxide Surfactant Sheets: Wrinkles, Overlaps and Impacts on Thin Film Properties. *Soft Matter* **2010**, *6*, 6096−6101.

(17) Zhang, X.; Sun, H.; Yang, S. Self-Limiting Assembly of Two-Dimensional Domains from Graphene Oxide at the Air/Water Interface. *J. Phys. Chem. C* **2012**, *116*, 19018−19024.

(18) Zheng, Q.; Ip, W. H.; Lin, X.; Yousefi, N.; Yeung, K. K.; Li, Z.; Kim, J.-K. Transparent Conductive Films Consisting of Ultralarge Graphene Sheets Produced by Langmuir−Blodgett Assembly. *ACS Nano* **2011**, *5*, 6039−6051.

(19) Kovtyukhova, N. I.; Ollivier, P. J.; Martin, B. R.; Mallouk, T. E.; Chizhik, S. A.; Buzaneva, E. V.; Gorchinskiy, A. D. Layer-by-Layer Assembly of Ultrathin Composite Films from Micron-Sized Graphite Oxide Sheets and Polycations. *Chem. Mater.* **1999**, *11*, 771−778.

(20) Hummers, W. S.; Offeman, R. E. Preparation of Graphitic Oxide. *J. Am. Chem. Soc.* **1958**, *80*, 1339−1339.

(21) Matsumoto, Y.; Koinuma, M.; Kim, S. Y.; Watanabe, Y.; Taniguchi, T.; Hatakeyama, K.; Tateishi, H.; Ida, S. Simple Photoreduction of Graphene Oxide Nanosheet under Mild Conditions. *ACS Appl. Mater. Interfaces* **2010**, *2*, 3461−3466.

(22) Li, D.; Muller, M. B.; Gilje, S.; Kaner, R. B.; Wallace, G. G. Processable Aqueous Dispersions of Graphene Nanosheets. *Nat. Nanotechnol.* **2008**, *3*, 101−105.

(23) Paredes, J. I.; Villar-Rodil, S.; Martínez-Alonso, A.; Tascón, J. M. D. Graphene Oxide Dispersions in Organic Solvents. *Langmuir* **2008**, *24*, 10560−10564.

(24) Park, S.; An, J.; Piner, R. D.; Jung, I.; Yang, D.; Velamakanni, A.; Nguyen, S. T.; Ruoff, R. S. Aqueous Suspension and Characterization of Chemically Modified Graphene Sheets. *Chem. Mater.* **2008**, *20*, 6592−6594.

(25) Kim, J.; Cote, L. J.; Kim, F.; Yuan, W.; Shull, K. R.; Huang, J. Graphene Oxide Sheets at Interfaces. *J. Am. Chem. Soc.* **2010**, *132*, 8180−8186.

(26) Kim, J.; Kim, F.; Huang, J. Seeing Graphene-Based Sheets. *Mater. Today* **2010**, *13*, 28−38.

(27) Acik, M.; Lee, G.; Mattevi, C.; Chhowalla, M.; Cho, K.; Chabal, Y. J. Unusual Infrared-Absorption Mechanism in Thermally Reduced Graphene Oxide. *Nat. Mater.* **2010**, *9*, 840−5.

(28) Lerf, A.; He, H.; Forster, M.; Klinowski, J. Structure of Graphite Oxide Revisited. *J. Phys. Chem. B* **1998**, *102*, 4477−4482.

(29) Szabó, T.; Berkesi, O.; Forgó, P.; Josepovits, K.; Sanakis, Y.; Petridis, D.; Dékány, I. Evolution of Surface Functional Groups in a Series of Progressively Oxidized Graphite Oxides. *Chem. Matter* **2006**, *18*, 2740−2749.

(30) Elimelech, M.; Gregory, J.; Jia, X.; Williams, R. *Particle Deposition and Aggregation;* BH: Oxford, U.K. 1995.

(31) Trizac, E.; Bocquet, L.; Agra, R.; Weis, J.; Aubouy, M. Effective Interactions and Phase Behaviour for a Model Clay Suspension in an Electrolyte. *J. Phys.: Condens. Mater.* **2002**, *14*, 9339.

(32) Gregory, J. The Effect of Cationic Polymers on the Colloidal Stability of Latex Particles. *J. Colloid Interface Sci.* **1976**, *55*, 35−44.

(33) Hamaker, H. C. The London—Van Der Waals Attraction between Spherical Particles. *Physica* **1937**, *4*, 1058−1072.

(34) McAllister, M. J.; Li, J.-L.; Adamson, D. H.; Schniepp, H. C.; Abdala, A. A.; Liu, J.; Herrera-Alonso, M.; Milius, D. L.; Car, R.; Prud'homme, R. K.; Aksay, I. A. Single Sheet Functionalized Graphene by Oxidation and Thermal Expansion of Graphite. *Chem. Mater.* **2007**, *19*, 4396−4404.

(35) Imperiali, L.; Liao, K. H.; Clasen, C.; Fransaer, J.; Macosko, C. W.; Vermant, J. Interfacial Rheology and Structure of Tiled Graphene Oxide Sheets. *Langmuir* **2012**, *28*, 7990−8000.

(36) Teschke, O.; Ceotto, G.; de Souza, E. F. Interfacial Water Dielectric-Permittivity-Profile Measurements Using Atomic Force Microscopy. *Phys. Rev. E* **2001**, *64*, 011605.

(37) Cheng, J.; Vecitis, C. D.; Hoffmann, M. R.; Colussi, A. J. Experimental Anion Affinities for the Air/Water Interface. *J. Phys. Chem. B* **2006**, *110*, 25598−25602.

(38) Crocker, J.; Grier, D. Microscopic Measurement of the Pair Interaction Potential of Charge-Stabilized Colloid. *Phys. Rev. Lett.* **1994**, *73*, 352−355.

(39) Israelachvili, J.; Pashley, R. The Hydrophobic Interaction Is Long Range, Decaying Exponentially with Distance. *Nature* **1982**, *300*, 341−342.

(40) Golestanian, R.; Goulian, M.; Kardar, M. Fluctuation-Induced Interactions between Rods on a Membrane. *Phys. Rev. E* **1996**, *54*, 6725−6734.

(41) Botto, L.; Lewandowski, E. P.; Cavallaro, M.; Stebe, K. J. Capillary Interactions between Anisotropic Particles. *Soft Matter* **2012**, *8*, 9957−9971.

(42) Loudet, J. C.; Alsayed, A. M.; Zhang, J.; Yodh, A. G. Capillary Interactions between Anisotropic Colloidal Particles. *Phys. Rev. Lett.* **2005**, *94*, 018301.

(43) Danov, K. D.; Kralchevsky, P. A. Interaction between Like-Charged Particles at a Liquid Interface: Electrostatic Repulsion Vs. Electrocapillary Attraction. *J. Colloid Interface Sci.* **2010**, *345*, 505−514.

(44) Nikolaides, M. G.; Bausch, A. R.; Hsu, M. F.; Dinsmore, A. D.; Brenner, M. P.; Gay, C.; Weitz, D. A. Electric-Field-Induced Capillary Attraction between Like-Charged Particles at Liquid Interfaces. *Nature* **2002**, *420*, 299−301.

(45) Šiber, A.; Ziherl, P. Many-Body Contact Repulsion of Deformable Disks. *Phys. Rev. Lett.* **2013**, *110*, 214301.

(46) Foret, L.; Würger, A. Electric-Field Induced Capillary Interaction of Charged Particles at a Polar Interface. *Phys. Rev. Lett.* **2004**, *92*, 058302.